Aeroacoustics Conferences
26-29 May 2026, Brussels, Belgium
32nd AIAA/CEAS Aeroacoustics Conference (2026)
10.2514/6.2026-3395

Experimental and Numerical Analysis of Tonal and Broadband Noise in an Aeronautical Fan Stage

Jean Al-Am*
School of Aviation, Australian University, Safat 13015, West Mishref, Kuwait
École Centrale de Lyon, CNRS, Université Claude Bernard Lyon 1, INSA Lyon, LMFA, UMR5509, 69130, Ecully, France

Antonio Pereira, Alexis Giauque, Edouard Salze, Vincent Clair, Christoph Brandstetter, and Jérôme Boudet
École Centrale de Lyon, CNRS, Université Claude Bernard Lyon 1, INSA Lyon, LMFA, UMR5509, 69130, Ecully, France

Fernando Gea-Aguilera
Safran Aircraft Engines, 77550 Moissy-Cramayel, France

In this study, broadband and tonal noise of an Ultra–High Bypass Ratio (UHBR) fan and Outlet Guide Vanes (OGV) stage, developed at École Centrale de Lyon, are investigated using wall-modeled Large Eddy Simulations (LES) and compared with experimental measurements. A full-annulus (360°) wall-modeled LES of the complete fan/OGV stage was carried out at approach conditions, which is an important operating point for aircraft noise certification. The fully compressible LES was performed on a finely resolved unstructured grid, enabling the direct computation of both aerodynamic and acoustic fields. The LES predictions are validated against experimental data in terms of aerodynamic performance and acoustic behavior. Good agreement is obtained for key aerodynamic parameters, confirming the accuracy of the simulated operating point. Comparisons of broadband noise spectra and tonal noise components further demonstrate the ability of the LES to reproduce the main acoustic features observed experimentally. The use of a 360° LES configuration allows for the full azimuthal modal content of the fan noise to be captured, which cannot be achieved with conventional periodic sector LES simulations commonly employed in the literature. The resulting modal analysis shows that the 360° LES successfully retrieves the experimental modal distribution of the fan stage at approach conditions, confirming its capability as a predictive tool for fan noise studies.

I. Nomenclature

Acronyms

LES	Large Eddy Simulation
RANS	Reynolds-Averaged Navier–Stokes
OGV	Outlet Guide Vane
NSCBC	Navier–Stokes Characteristic Boundary Conditions
TTGC	Two-step Taylor–Galerkin Convection
UHBR	Ultra-High Bypass Ratio
BPF	Blade Passing Frequency
PSD	Power Spectral Density

*Corresponding author. j.alam@au.edu.kw

Roman Letters

A^{+}_{mj}	Downstream propagating modal amplitude [Pa]
A^{-}_{mj}	Upstream propagating modal amplitude [Pa]
B	Blade count [-]
c_0	Speed of sound [m/s]
c_r	Rotor chord length [m]
f	Frequency [Hz]
f_c	Mesh cut-off frequency [Hz]
f_{mj}	Radial mode shape function [-]
H	Relative height [-]
I_a	Acoustic intensity [W/m^2]
j	Radial mode order [-]
k_{mj}	Axial wavenumber of mode (m, j) [rad/m]
k_t	Turbulence kinetic energy [m^2/s^2]
K_{mj}	Eigenvalue of duct mode (m, j) [-]
m	Azimuthal mode order [-]
M	Mach number [-]
$\dot{m}$	Mass flow rate [kg/s]
P	Static pressure [Pa]
P_0	Total pressure [Pa]
P_{tot}	Total pressure downstream of the fan [Pa]
p'	Pressure fluctuations [Pa]
Q	Q-criterion [s^{-2}]
S_{ij}	Symmetric velocity gradient tensor [s^{-1}]
t	Time [s]
T_0	Total temperature [K]
T_{tot}	Total temperature downstream of the fan [K]
u	Streamwise velocity component [m/s]
$\bar{u}$	Mean velocity [m/s]
u^+	Dimensionless wall velocity [-]
U	Velocity magnitude [m/s]
V	Vane count [-]
V_r	Radial velocity component [m/s]
V_x	Axial velocity component [m/s]
V_θ	Azimuthal velocity component [m/s]
x, y, z	Cartesian coordinates [m]
x^+, y^+, z^+	Dimensionless wall distances [-]
Ω_{ij}	Antisymmetric velocity gradient tensor [s^{-1}]

Greek Letters

β	Relative flow angle [°]
γ	Ratio of specific heats [-]
Δt	Time step [s]
λ_{ac}	Acoustic wavelength [m]
ν	Kinematic viscosity [m^2/s]
ρ	Density [kg/m^3]
ω	Angular frequency [rad/s]
ω_c	Cut-off angular frequency [rad/s]
Ω	Rotation speed [RPM]
Ω_n	Nominal rotation speed [RPM]

II. Introduction

With the strengthening of international aviation regulations, aero-engine manufacturers are increasingly required to reduce both CO_2 and noise emissions while improving overall engine efficiency. To meet these demands, modern aero-engines, such as Ultra–High Bypass Ratio (UHBR) turbofan engines, feature larger fan diameters and higher bypass ratios. As a result, one of the main contributors to the overall engine noise is the fan–Outlet Guide Vane (OGV) stage [1, 2]. The fan/OGV stage noise consists of both tonal and broadband noise components.

Tonal noise arises from periodic interactions within the fan stage and depends directly on the number of blades and vanes. It typically occurs at the Blade Passing Frequency (BPF) and its harmonics. Tonal noise mechanisms have been extensively studied using analytical, numerical, and experimental approaches [1, 2]. Various noise mitigation strategies have been proposed, including optimizing blade–vane count ratios to account for duct mode cut-off effects [3], as well as implementing acoustic liners in inlet and exhaust ducts [4].

Broadband noise originates from stochastic and turbulent flow mechanisms within the fan stage and remains less well documented in the literature. The main broadband sources include blade tip-leakage vortex noise, trailing-edge noise, separation noise, and rotor–stator interaction noise. Tip-leakage vortex noise primarily results from the interaction between the unsteady gap flow - developing between the blade tip and casing - and either the trailing-edge corner or neighboring blades [5]. Trailing-edge noise is associated with the diffraction of turbulent boundary layers at blade and vane trailing edges [6]. Separation noise arises from pressure and velocity fluctuations caused by flow separation near the leading edges at low fan speeds [7]. The rotor–stator interaction noise, which is considered to be dominant at approach conditions [8, 9], is generated by the interaction between rotor wake turbulence and OGV leading edges, resulting in unsteady loading on the vanes [10]. In recent decades, several analytical and numerical methods have been developed to model and predict these broadband noise mechanisms [2, 11, 12].

To design and optimize noise-reduction technologies, the underlying noise-generation mechanisms must be clearly understood [2, 13, 14]. Both experimental and numerical approaches are therefore being advanced to analyze the complex flow–acoustic interactions within fan stages. Among these, modal analysis of the ducted acoustic field has emerged as a particularly promising technique [15–19]. Modal characterization enables the identification of the most energetic propagating modes, their frequency ranges, and direction of propagation. In practice, such modal detection supports the development of active control systems capable of targeting and mitigating dominant acoustic modes [1, 20, 21].

In the present work, the flow field and acoustic emissions of a fan/OGV stage are investigated using a full-annulus (360°) Large Eddy Simulation (LES). The numerical setup is carefully designed to ensure (i) an accurate representation of turbulent structures within the boundary layers and wakes, and (ii) a realistic propagation of acoustic waves throughout the fan stage. The main objective of this study is to validate the complete acoustic modal content obtained directly from the LES, both upstream and downstream of the fan stage, by comparison with experimental measurements.

The paper is organized as follows. Section III describes the fan/OGV configuration and the numerical setup used for the LES. Sections IV and V present a comparison between the numerical predictions and experimental data in terms of mean flow and broadband and tonal noise emissions. In Section VI, The modal content of the acoustic field, obtained via azimuthal and radial modal decomposition of the 360° LES results, will be analyzed and compared with the experimental observations. Finally, the main conclusions are presented in Section VII.

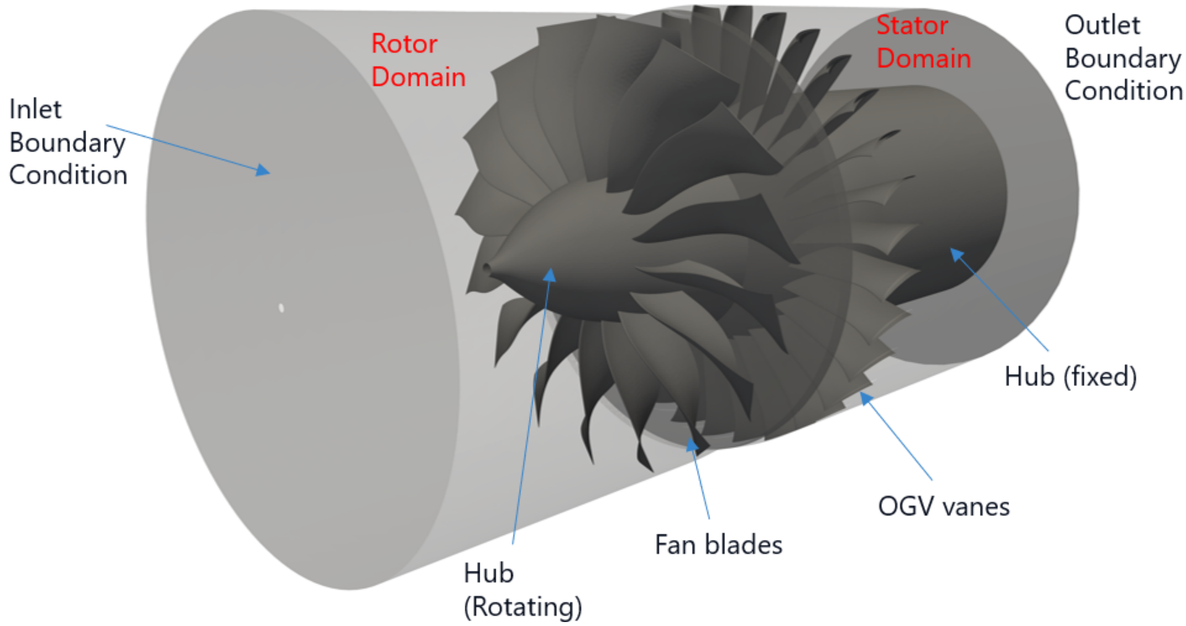

Fig. 1 Computational domains of the 360° ECL5 fan/OGV stage.

III. Numerical Setup

A. Computational Domain

The configuration investigated in this study is the ECL5 fan/OGV stage, designed at École Centrale de Lyon [22] based on the technical requirements of a mid-range commercial aircraft. The ECL5 represents a new open test case corresponding to an UHBR aero-engine, operating at a low rotational speed and without core flow. The fan stage consists of $B = 16$ fan blades and $V = 31$ OGVs.

The computational domain for the full-annulus (360°) LES configuration is shown in Figure 1. The simulation is performed using the AVBP solver [23], developed by CERFACS. This solver requires identical angular extents for the rotor and stator domains. Consequently, the 360° LES enables modeling of the exact blade–vane configuration of the ECL5 stage, whereas a periodic-sector LES would require modification of the vane count to satisfy periodicity constraints [5, 7, 24]. The computational domain extends from 3.75 fan chord lengths upstream of the rotor leading edge to 4.25 vane chord lengths downstream of the stator trailing edge. The upstream extent is selected to ensure the development of a fully established boundary layer along the casing.

The simulation is conducted at approach conditions, corresponding to a rotational speed of $\Omega = 6050$ rpm, which represents 55% of the nominal rotational speed (Ω_n), and leads to a BPF of 1613.13 Hz for this configuration.

B. LES Numerical Parameters

In the present study, the AVBP solver [23, 25] is employed to solve the governing equations of the LES. AVBP is an explicit, unstructured, and fully compressible LES solver. For this turbomachinery application, two computational domains are used: the *rotor domain*, containing the fan blades, and the *stator domain*, containing the OGVs. The two domains are coupled through the CWIPI coupling library, which relies on an overset (overlapping) grid method [26].

The convective terms of the filtered Navier–Stokes equations are discretized using the Two-step Taylor–Galerkin (TTGC) scheme [27], a third-order finite-volume method. The unresolved turbulent scales are modeled with the SIGMA subgrid-scale model [28]. At the inlet and outlet boundaries, non-reflecting Navier–Stokes Characteristic Boundary Conditions (NSCBC) [29] are applied. A uniform mean flow is injected axially at the inlet with a total pressure of $P_0 = 101{,}325$ Pa and a total temperature of $T_0 = 300$ K. The static pressure at the outlet is adjusted to achieve the desired mass flow rate through the fan stage.

No-slip boundary conditions are imposed on all solid surfaces, including blades, vanes, hub, and shroud walls. The

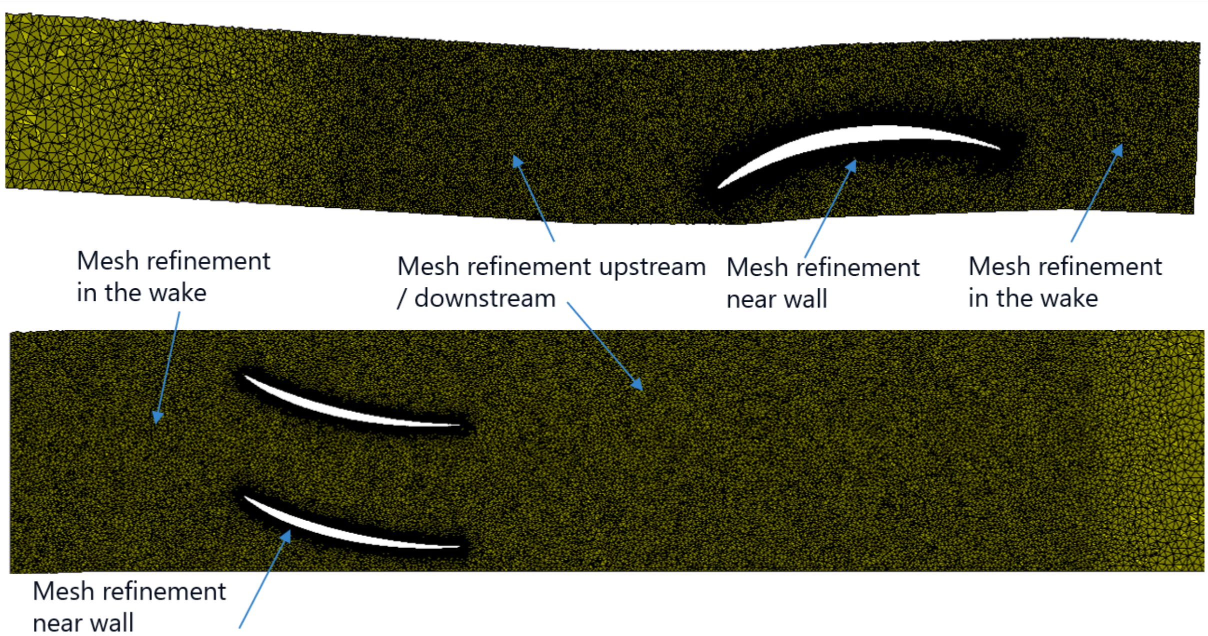

Fig. 2 Grid in a blade-to-blade view at mid-span. The rotor domain is shown in the top view, and the stator domain is presented in the bottom view.

Table 1 Mesh properties of the LES grid. x^+, y^+ and z^+ denote the maximum dimensionless wall distances in the streamwise, wall-normal, and spanwise directions, respectively.

	360° LES
Number of cells [10^6]	1500
x^+/z^+	150
y^+	25
Number of prism layers	10
Expansion ratio	1.1
Time step [10^{-8}s]	2.8
CPUh/blade passage [10^3]	1700

near-wall region is modeled using a logarithmic wall law [30], expressed as,

$$u^+ = \frac{1}{\kappa}\ln(Ay^+) \quad \text{for } y^+ > 11.45, \tag{1}$$

where $\kappa = 0.41$ and $A = 9.2$. For the dimensionless wall distance $y^+ \leq 11.45$, a linear relation is imposed ($u^+ = y^+$).

The LES time step is set to $\Delta t = 2.8\times10^{-8}$ s, corresponding to a computational cost of approximately 1.7×10^6 CPUh per fan rotation. The simulation includes three full fan rotations to ensure numerical and statistical convergence, followed by six additional rotations for post-processing and acoustic data collection.

C. Mesh Characteristics

The grid at mid-span around the rotor blades and stator vanes is illustrated in Figure 2. The computational mesh is an unstructured hybrid grid composed of several element types: prismatic cells in the near-wall regions (on the blade, vane, shroud, and hub surfaces), tetrahedral cells in the outer flow regions, and pyramidal cells in the transition zones between these regions. The mesh is designed to provide adequate resolution of boundary-layer and wake turbulence, while ensuring accurate propagation of acoustic waves through the fan stage with minimal numerical dissipation and dispersion. An unstructured hybrid mesh is employed since the AVBP solver's finite-volume scheme is formulated for unstructured grids, allowing accurate flux computation and efficient LES on the complex geometry of rotor and stator domains.

The main mesh characteristics for the 360° LES are summarized in Table 1. Near-wall refinement follows predefined dimensionless cell sizes, denoted by x^+, y^+, and z^+ in the streamwise, wall-normal, and spanwise directions, respectively. These values are chosen to meet the criteria established in Ref. [31], ensuring that local resolutions remain within acceptable limits. The smallest spacing is applied to the first prismatic layer adjacent to the wall, followed by a gradual increase in cell size through a controlled expansion ratio.

In the upstream and downstream regions, mesh density is determined using both turbulent and acoustic resolution criteria introduced by the authors in Ref. [31]. For the acoustic criterion, at least 13 points per wavelength are used, with the acoustic wavelength defined as,

$$\lambda_{ac} = \frac{c_0(1-M)}{f_c}, \tag{2}$$

where c_0 is the speed of sound, M the flow mean Mach number, and f_c = 12 kHz the target cut-off frequency. This criterion ensures accurate propagation of acoustic waves upstream of the rotor and downstream of the stator, up to the specified cut-off frequency.

To properly capture the turbulent structures in the rotor wakes, the local cell size is maintained below 50 times the Taylor microscale, defined as,

$$\lambda_{Ta} = \left(10\frac{\nu k_t}{\epsilon}\right)^{1/2}, \tag{3}$$

where ν is the kinematic viscosity, k_t the turbulence kinetic energy, and ϵ the turbulence dissipation rate. These acoustic- and turbulence-based refinement criteria depend on the numerical scheme and mesh topology, and have been demonstrated to yield accurate results in previous studies [5, 31].

IV. Aerodynamics

A. Instantaneous Flow Quantities

First, the instantaneous flow around the rotor blades and stator vanes is analyzed. Figure 3 presents iso-contours of the Q-criterion ($Qc_r^2/U^2 = 15$, where U is the inflow velocity magnitude and c_r is the chord length at mid-span of the rotor blade) obtained from the 360° LES. The Q-criterion is defined as,

$$Q = \frac{1}{2}\left(\Omega_{ij}\Omega_{ij} - S_{ij}S_{ij}\right), \tag{4}$$

where S_{ij} and Ω_{ij} are the symmetric and antisymmetric parts of the velocity gradient tensor $\partial u_i/\partial x_j$, respectively, given by

$$S_{ij} = \frac{1}{2}\left(\frac{\partial u_i}{\partial x_j} + \frac{\partial u_j}{\partial x_i}\right), \qquad \Omega_{ij} = \frac{1}{2}\left(\frac{\partial u_i}{\partial x_j} - \frac{\partial u_j}{\partial x_i}\right), \tag{5}$$

where u_i corresponds to the velocity component in the i-th direction, and x_j denotes the spatial coordinate in the j-th direction. The Einstein summation convention over repeated indices is implied. Positive values of Q correspond to rotation-dominated regions, typically associated with vortical structures.

The iso-surfaces of the Q-criterion are colored by the vorticity magnitude. Turbulent structures of various scales are observed within the boundary layers of the blades and vanes, as well as in the wake regions. Boundary-layer transition is clearly visible near the leading edges of both the rotor blades and the stator vanes along the entire span. This observation is consistent with previous LES studies of fan stages operating at approach conditions [32].

The small-scale turbulent structures downstream of the transition regions are directly responsible for the generation of trailing-edge noise, as these eddies are scattered by the trailing edges of the blades and vanes. In contrast, the rotor-stator broadband interaction noise arises from the interaction between the turbulent structures in the rotor wakes and the leading edges of the stator vanes.

The iso-contours of the Q-criterion are presented together with contours of the instantaneous dilatation rate, $\nabla \cdot \mathbf{u}$, at 99% of the rotor span. Distinct acoustic wave fronts are observed propagating both upstream and downstream of the fan stage, demonstrating the capability of the 360° LES to accurately capture noise generation and propagation within the refined mesh region. It should be noted that no spurious sound reflections arise from either the upstream or downstream boundaries of the computational domain, confirming the effectiveness of the applied boundary conditions.

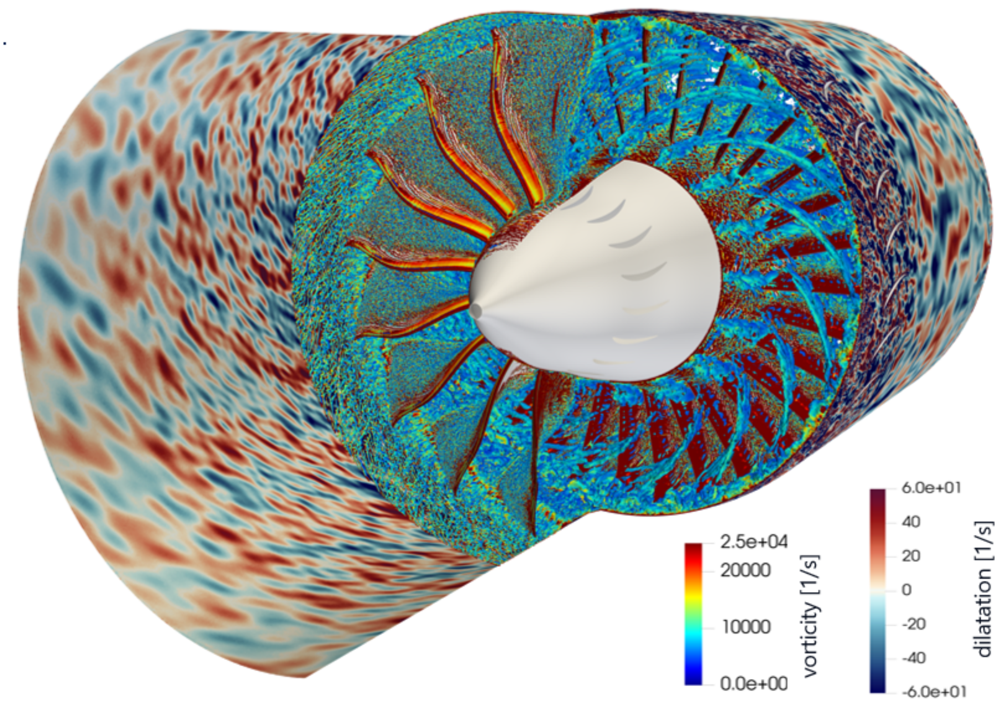

Fig. 3 Iso-contours of Q-criterion colored by vorticity magnitude in the fan stage, and instantaneous contours of dilatation rate at 99% of the span, obtained by the 360° LES.

Table 2 Fan stage performance at approach condition.

	Experimental data	RANS	LES
$\dot{m}$ [kg/s]	22.00	22.00	21.98 (-0.09%)
P_{tot}/P_0	1.0863	1.0839 (-0.22%)	1.0849 (-0.13%))
η	0.9072	0.9064 (-0.088%)	0.9058 (-0.15%)

B. Averaged Quantities

The LES results are initially compared with the available performance and aerodynamic experimental data. The performance parameters, namely the mass flow rate $\dot{m}$, the total pressure ratio P_{tot}/P_0, and the isentropic efficiency η, obtained from the Reynolds-Averaged Navier-Stokes (RANS) simulations, LES, and experimental measurements, are summarized in Table 2. The results from the RANS simulation were obtained from a previous work [22], in which further details on the mesh and numerical setup are provided. These quantities are computed as mass-flow-rate-weighted averages over axial planes located at two chord lengths upstream of the fan at blade mid-span and two chord lengths downstream of the OGVs at vane mid-span.. The LES predictions show good agreement with the experimental data. Minor discrepancies are observed for the mass flow rate (-0.09%), the total pressure ratio (-0.13%), and the isentropic efficiency (-0.15%). These small deviations confirm the accuracy of the LES setup and validate the operating point used in the simulation.

The radial distributions of the total pressure ratio, the relative flow angle β, and the total temperature difference $(T_{\text{tot}} - T_0)$ in the interstage region are compared in Figure 4. Both the RANS and LES simulations show good qualitative agreement near the hub ($H < 10\%$) and the shroud ($H > 90\%$). The influence of corner separation near the hub can be found between 0% and 10% of the channel height, where increases in P_{tot}/P_0 and $(T_{\text{tot}} - T_0)$, together with a decrease in β, can be observed. Tip flow effects appear between 90% and 100% of the channel height, characterized by a decrease in P_{tot}/P_0, and increases in β and $(T_{\text{tot}} - T_0)$ values. The total pressure profiles show good agreement among all approaches. The relative flow angle β is better captured by the LES compared to the RANS, with only small discrepancies near the hub and tip regions. The RANS simulation tends to underpredict the flow angles across the span

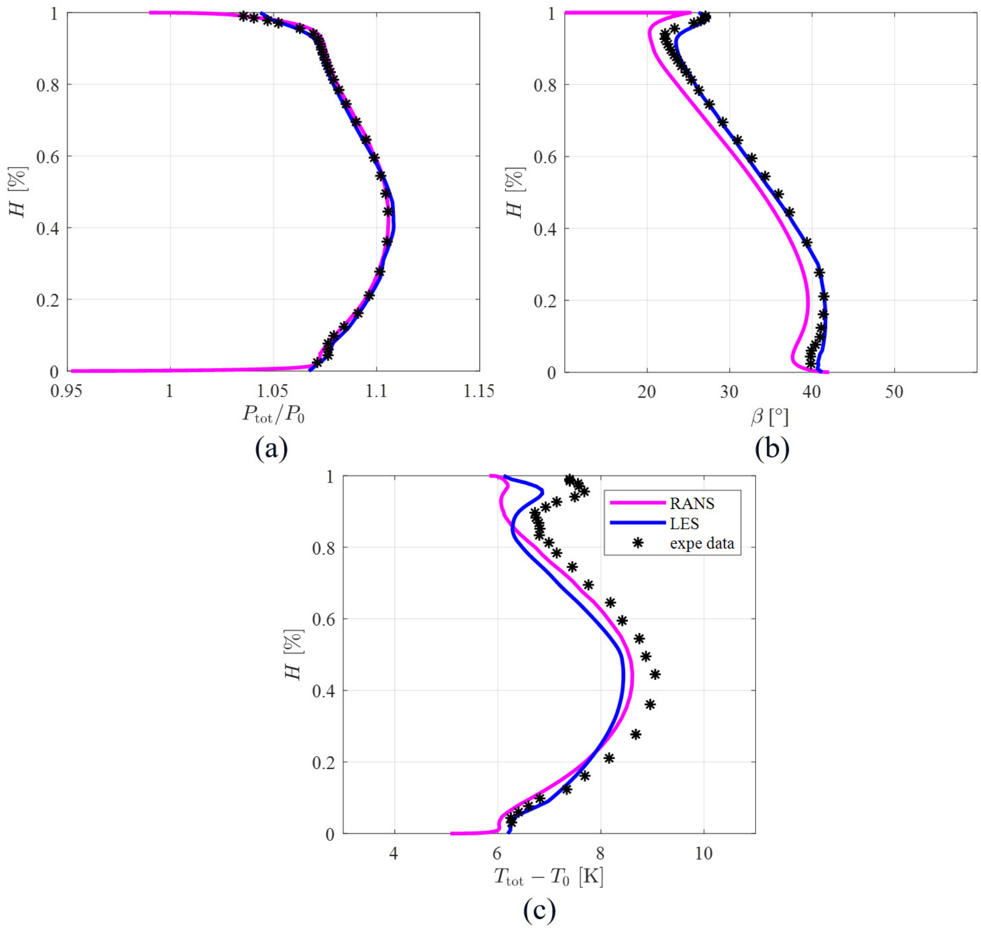

Fig. 4 Comparison between the LES, RANS [22] and experimental results of the radial profiles of the (a) total pressure, (b) relative flow angle, and (c) total temperature difference in the interstage.

relative to the experimental data. Both LES and RANS predict slightly lower total temperatures than the measurements, starting at approximately 20% of the channel height. Additionally, in the tip region the LES predicts a better $(T_{tot} - T_0)$ profile than the RANS result, which is essential for fan noise prediction, as the tip region is considered as an important noise source.

V. Noise Prediction

In this section, the noise spectra from the fan stage are predicted directly from the 360° LES domain and compared to experimental data.

Figure 5 presents a comparison of the Power Spectral Density (PSD) between the LES results and experimental measurements at two axial positions: Plane 110, which is located approximately one mid-span rotor chord length upstream of the fan blades, and Plane 150, located approximately one mid-span stator chord length downstream of the stator vanes. Results are circumferentially averaged using 200 monitor probes for the LES and 8 microphones for the experimental data. For the LES, the time signal covers six full rotor rotations, whereas for the experimental data, it corresponds to approximately 30,000 full rotations, which corresponds to 5 minutes of acquisition. The PSD is computed using a Hanning window with 50% overlap, and the length of the segment corresponds to a frequency resolution of $\Delta f = 150$ Hz for the LES data. The mesh cut-off frequency for the LES is shown by the dashed vertical line in Figure 5, and is defined as $f_c = \frac{c_0 - V_0}{13 * \Delta x}$, where Δx is the mesh size in the acoustic propagation region, c_0 is the speed of sound, and V_0 is the inflow axial velocity. For the present simulation, f_c corresponds to approximately 12 kHz. The broadband component from the 360° LES is obtained by performing a phase average over 96 blade-passing periods.

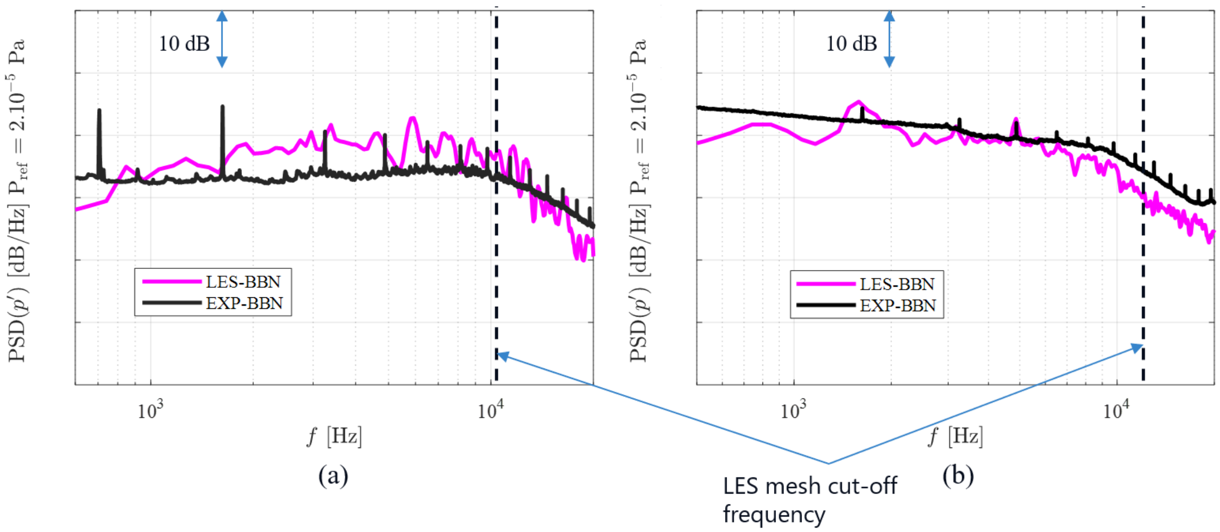

Fig. 5 Comparison of the PSD of the pressure fluctuations, p', between the LES and the experimental data. (a) Upstream of the fan blades at Plane 110. (b) Downstream of the OGVs at plane 150.

This approach allows direct extraction of the tonal component, which is then subtracted from the total noise in the time domain to isolate the broadband noise. A similar process is applied to the experimental data. A tachometer probe records a one-pulse-per-revolution signal, which is used to resample the microphone data from the time domain to the angular domain. An integer number of samples per revolution is obtained, and the tonal noise is then determined by averaging over approximately 760 periods, each consisting of 40 rotor revolutions. Experimentally, this procedure may result in some residual peaks at the BPFs (first harmonic of the BPF is 1613.13Hz), as it can be seen Figure 5, but at levels significantly lower than the main tonal contributions at these frequencies.

Overall, the comparison between the LES and the experimental spectra shows good agreement. At the upstream plane (Figure 5 left), the LES slightly underpredicts the sound levels for frequencies below 1000 Hz, which may be attributed to the limited LES sampling duration affecting the low-frequency content. Between 3000 Hz and 7000 Hz, the LES overpredicts the sound levels by approximately 2 to 5 dB relative to the experimental data. This difference is likely associated with tip-leakage noise, which originates from the interaction between the tip-leakage vortex and the blade trailing edges, and may occur in this frequency range, particularly upstream [5]. The differences observed in Figure 4 in the tip region suggest that the tip-leakage vortex is not reproduced identically in the LES and the experiment, which may partly explain the observed deviations in the corresponding noise levels. At the downstream plane (Figure 5 right), a similarly good agreement is observed between LES and experiment. The LES slightly underpredicts the sound levels by around 1 dB at low and mid frequencies, and by about 2 dB near the mesh cut-off frequency. As expected when broadband interaction noise is dominant, the overall sound levels are higher downstream than upstream, and this trend is well captured by the 360° LES simulation. It should be noted that the peak observed in the upstream PSD (Figure 5, left) just above 700 Hz is not affected by the phase averaging procedure applied to extract the broadband noise. This noise contribution appears only upstream of the fan stage and does not seem to be associated with the rotational velocity of the stage.

The tonal noise levels at BPF1 are compared between the LES and experimental data in Figure 6 at Plane 110 and 150. For the numerical case, 200 monitoring probes are equally distributed in the azimuthal direction and the tonal noise is obtained using a phase average over 96 blade passages. For the experimental measurements, 8 microphones are used at Plane 110 and 15 microphones at Plane 150, where the microphones are not located at a constant axial position.

The LES results exhibit small azimuthal variations, on the order of approximately 1 dB. These oscillations can partly be attributed to rotor-stator interaction noise, and may also be influenced by the finite sampling duration of the LES and by minor inhomogeneities in the computational mesh. Nevertheless, the amplitude of these oscillations remains limited, which indicates that the mesh quality and numerical setup are satisfactory. In contrast, the experimental data show larger azimuthal variations, reaching up to 3 dB, at plane 150. These variations may be related to slight inflow non-uniformities along the azimuthal direction. Overall, good agreement is observed between the LES and

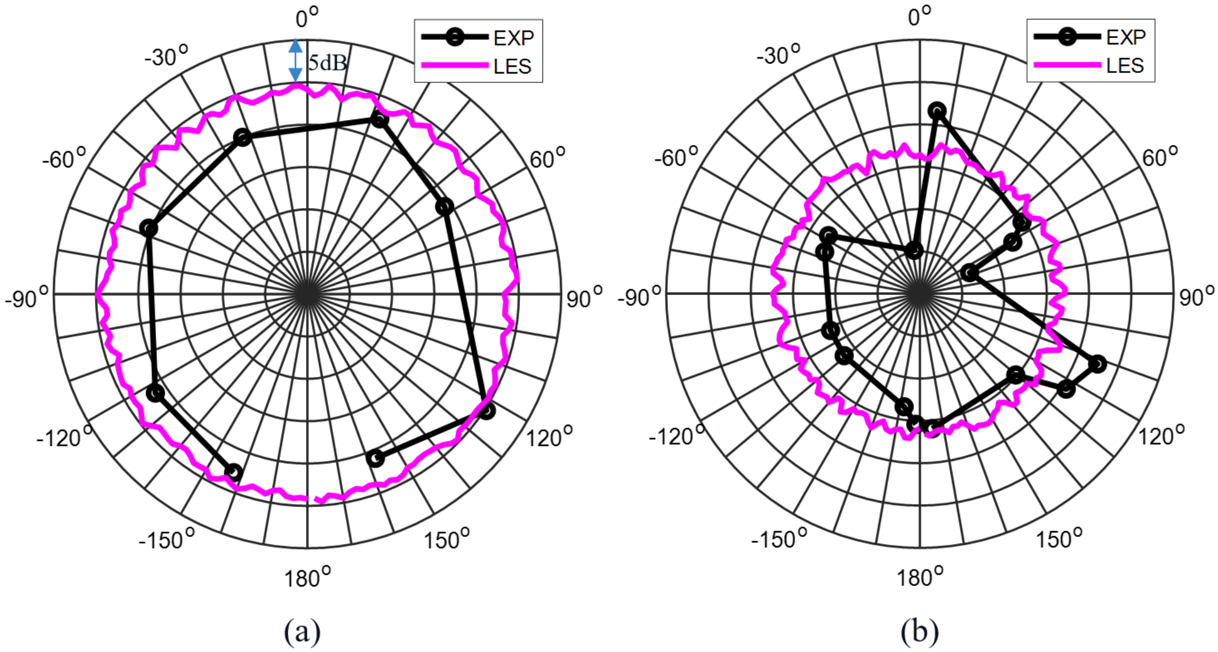

Fig. 6 Comparison of the azimuthal distribution of the tonal noise levels at BPF1 between the LES and the experimental data. (a) Upstream of the fan blades at Plane 110. (b) Downstream of the OGVs at plane 150.

the experimental measurements, although the LES slightly overpredicts the tonal levels at certain azimuthal positions, particularly at Plane 110. The differences between LES and experiment results range from approximately 0.5 to 4 dB at BPF1. These discrepancies remain within the variability observed across the different azimuthal positions in the experimental results.

At Plane 150, the azimuthal variations in the experimental data are more pronounced than those observed at Plane 110. This may partly result from small differences in the axial positioning of the sensors at this location. Additionally, these variations may also be attributed to the downstream supporting struts, which can generate correlated upstream-propagating modes, as well as to the presence of multiple interacting radial modes of the same azimuthal order, leading to axial variations in the pressure field. The LES results display similar azimuthal trends at Plane 150 as those observed at Plane 110. The LES tonal noise levels generally fall within the envelope defined by the minimum and maximum experimental levels. Overall, the comparison of tonal noise demonstrates an acceptable level of agreement between the LES predictions and the experimental data.

VI. Modal Content

One of the main advantages of the 360° LES, compared to a periodic-sector LES, is its ability to perform a complete azimuthal decomposition of the acoustic field radiated by the fan stage. By assuming linear acoustic behavior, a uniform flow Mach number, and wave propagation in a rigid-walled annular duct, the acoustic pressure $p'(r,\theta,x,t)$ obtained from the solution of the advected Helmholtz equation can be expressed as a weighted sum of modes [33]:

$$p'(r,\theta,x,t) = \sum_{m=-\infty}^{\infty} \sum_{j=0}^{\infty} \left(A_{mj}^{+} e^{\mathrm{i}k_{mj}^{+}x} + A_{mj}^{-} e^{\mathrm{i}k_{mj}^{-}x} \right) f_{mj}(r) e^{\mathrm{i}m\theta} e^{-\mathrm{i}\omega t}, \tag{6}$$

where A_{mj}^{+} and A_{mj}^{-} are the modal amplitudes of waves propagating in the downstream and upstream directions, respectively. Here, ω is the angular frequency, and the subscripts m and j denote the azimuthal and radial mode orders. The axial wavenumbers in the downstream (+) and upstream (-) directions are denoted by $k_{mj}^{\pm}$, and $f_{mj}(r)$ is the normalized radial modal function, which is a solution of the Bessel equations of the first and second kind. The radial function $f_{mj}(r)$ depends only on the cross-sectional geometry of the annular duct and the radial boundary conditions. Expressions for the axial wavenumbers and radial functions can be found in Ref. [33].

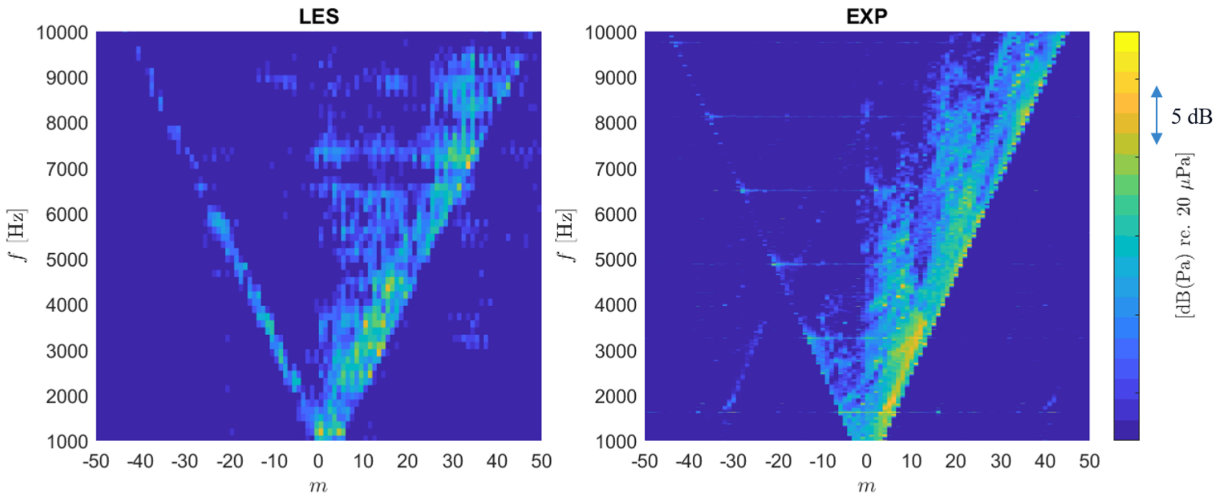

(a) (b)

Fig. 7 Azimuthal mode detection plots at the intake section obtained from the (a) 360° LES and the (b) experimental data.

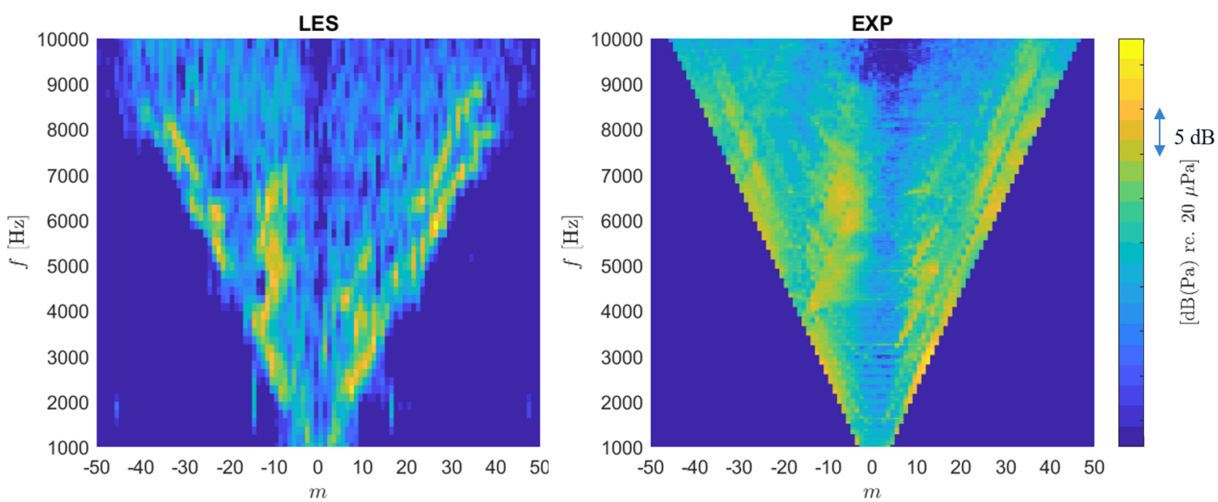

(a) (b)

Fig. 8 Azimuthal mode detection at the exhaust section. (a) 360° LES. (b) experimental data.

To compute the duct modes, 200 azimuthal monitoring positions are placed at one rotor chord length upstream of the rotor (intake section) and one stator chord length downstream of the stator (exhaust section). For each azimuthal position, 20 monitor points are used in the radial direction.

The azimuthal modal content at the intake and exhaust sections is obtained via azimuthal modal decomposition using the duct mode basis and compared between LES and experimental data in Figures 7 and 8. Overall, LES and experiments results show good agreement. The LES results exhibit greater scatter compared to the experimental data, which is likely due to the shorter sampling duration and limited temporal averaging. Modal energy is primarily confined within the cut-on region (the V-shaped domain), indicating strong attenuation of cut-off modes. Residual amplitudes can still be observed near BPF harmonics.

At the intake, both LES and experimental data show a clear dominance of co-rotating modes ($m > 0$), consistent with previous studies [18, 19]. This behavior is attributed to rotor–stator interaction noise generated at the stator leading edges, where the dipole orientation favors the excitation of co-rotating modes. Quantitatively, the LES underpredicts modal levels by approximately 3 dB for co-rotating modes and 1 to 2 dB for counter-rotating modes. The difference between co- and counter-rotating contributions ranges from 2 to 5 dB.

At the exhaust, no clear dominance of co- or counter-rotating modes is observed partly due to the axial mean flow downstream of the OGV. The cut-on region appears slightly steeper than the theoretical prediction. As frequency increases, successive radial modes become cut-on, producing a characteristic rippled structure in the modal distribution.

VII. Conclusions and Perspectives

In the present study, a 360° LES is performed to compute both the flow topology and the complete acoustic field in a fan/OGV stage. The ECL5 fan stage, designed by Ecole Centrale de Lyon and representative of an UHBR aeroengine configuration, is investigated both numerically and experimentally at approach conditions.

The complete modal content is obtained from both LES and experimental data, which enables a detailed analysis of broadband and tonal noise at the intake and exhaust sections. At the intake, a clear dominance of co-rotating modes is identified. At the exhaust, a characteristic rippled structure is observed, with increased modal amplitudes at frequencies where successive radial modes become cut-on. Good agreement is observed between LES and experimental results, confirming the capability of the simulation to accurately capture both aerodynamic and acoustic features.

The noise generated by a complete fan/OGV stage is thus directly predicted using LES for the first time. The mean flow topology, power spectral density of the pressure fluctuations, and acoustic modal content all show consistent trends with test measurements.

As future work, the 360° LES database can serve as a reference to extend analytical models towards modern turbofan configurations. It also provides a foundation for investigating more advanced operating conditions and next-generation propulsion systems, such as unducted turbofans, open rotors, and propellers.

Acknowledgments

This work was performed within the framework of the industrial chair ARENA (ANR-18-CHIN-0004-01) co-financed by Safran Aircraft Engines and the French National Research Agency (ANR), and is also supported by the Labex CeLyA of the Université de Lyon, operated by the French National Research Agency (ANR-11-LABX-0060/ ANR-16-IDEX-0005).

The computational resources were provided by a PRACE European award (project LESFAN, proposal No. 2021240101), GENCI (CINES, project number A0102A05039). Additionally, this work was granted access to the HPC resources of PMCS2I (Pôle de Modélisation et de Calcul en Sciences de l'Ingénieur de l'Information) of the École Centrale de Lyon, Écully, France.

Most of the post-processing was performed using Antares (release 1.16.0, https://www.cerfacs.fr/antares).

References

[1] Envia, E., "Fan noise reduction: an overview," *International Journal of Aeroacoustics*, Vol. 1, No. 1, 2002, pp. 43–64. https://doi.org/10.1260/1475472021502668.

[2] Moreau, S., "Turbomachinery noise predictions: present and future," *Acoustics*, Vol. 1, No. 1, 2019, pp. 92–116. https://doi.org/10.3390/acoustics1010008.

[3] Tyler, J., and Sofrin, T., "Axial flow compressor noise studies," *Society of Automotive Engineers Transactions*, Vol. 70, 1962, pp. 309–332. https://doi.org/10.4271/620532.

[4] Liu, X., Zhao, D., Guan, D., Becker, S., Sun, D., and Sun, X., "Development and progress in aeroacoustic noise reduction on turbofan aeroengines," *Progress in Aerospace Sciences*, Vol. 130, 2022, p. 100796. https://doi.org/https://doi.org/10.1016/j.paerosci.2021.100796.

[5] Al-Am, J., Clair, V., Giauque, A., Boudet, J., and Gea-Aguilera, F., "Aeroacoustic analysis of the tip-leakage flow of an Ultra High Bypass Ratio fan stage," *Physics of Fluids*, 2023. https://doi.org/https://doi.org/10.1063/5.0146143.

[6] Roger, M., and Moreau, S., "Back-scattering correction and further extensions of Amiet's trailing-edge noise model. Part 1: theory," *Journal of Sound and vibration*, Vol. 286, No. 3, 2005, pp. 477–506.

[7] Al-Am, J., Clair, V., Giauque, A., Boudet, J., and Gea-Aguilera, F., "On the effects of a separation bubble on fan noise," *Journal of Sound and Vibration*, Vol. 537, 2022. https://doi.org/10.1016/j.jsv.2022.117180.

[8] Peake, N., and Parry, A. B., "Modern challenges facing turbomachinery aeroacoustics," *Annual Review of Fluid Mechanics*, Vol. 44, 2012, pp. 227–248. https://doi.org/10.1146/annurev-fluid-120710-101231.

[9] Lewis, D., de Laborderie, J., Sanjosé, M., Moreau, S., Jacob, M. C., and Masson, V., "Parametric study on state-of-the-art analytical models for fan broadband interaction noise predictions," *Journal of Sound and Vibration*, Vol. 514, 2021. https://doi.org/10.1016/j.jsv.2021.116423.

[10] Amiet, R. K., "Acoustic radiation from an airfoil in a turbulent stream," *Journal of Sound and Vibration*, Vol. 41, No. 4, 1975, pp. 407–420. https://doi.org/10.1016/S0022-460X(75)80105-2.

[11] Moreau, S., and Roger, M., "Advanced noise modeling for future propulsion systems," *International Journal of Aeroacoustics*, Vol. 17, No. 6-8, 2018, pp. 576–599. https://doi.org/10.1177/1475472X18789005.

[12] Gea-Aguilera, F., Gill, J., and Zhang, X., "On the Effects of Fan Wake Modelling and Vane Design on Cascade Noise," *Journal of Sound and Vibration*, Vol. 459, 2019, p. 114859. https://doi.org/10.1016/j.jsv.2019.114859.

[13] Yangzhou, J., Wu, J., Ma, Z., and Huang, X., "Aeroacoustic sources analysis of wake-ingesting propeller noise," *Journal of Fluid Mechanics*, Vol. 962, 2023, p. A29. https://doi.org/10.1017/jfm.2023.295.

[14] Al-Am, J., Djedi, B., and Sedaghat, A., "Aeroacoustics effects of localized surface heating on wings for integrated thermal management," *Physics of Fluids*, Vol. 38, No. 2, 2026. https://doi.org/10.1063/5.0316225.

[15] Joppa, P., "Acoustic mode measurements in the inlet of a turbofan engine," *Journal of Aircraft*, Vol. 24, No. 9, 1987, pp. 587–593. https://doi.org/https://doi.org/10.2514/3.45482.

[16] Sarin, S., and Rademaker, E., "In-flight acoustic mode measurements in the turbofan engine inlet of Fokker 100 aircraft," *15th Aeroacoustics Conference*, 1993, p. 4414. https://doi.org/https://doi.org/10.2514/6.1993-4414.

[17] Sanjose, M., Daroukh, M., Magnet, W., De Laborderie, J., Moreau, S., and Mann, A., "Tonal fan noise prediction and validation on the ANCF configuration," *Noise Control Eng. J*, Vol. 63, No. 6, 2015, pp. 552–561.

[18] Casalino, D., Hazir, A., and Mann, A., "Turbofan broadband noise prediction using the lattice Boltzmann method," *AIAA Journal*, Vol. 56, No. 2, 2018, pp. 609–628. https://doi.org/10.2514/1.J055674.

[19] Pereira, A., and Jacob, M. C., "Modal analysis of in-duct fan broadband noise via an iterative Bayesian inverse approach," *Journal of Sound and Vibration*, Vol. 520, 2022. https://doi.org/https://doi.org/10.1016/j.jsv.2021.116633.

[20] Traub, P., Kennepohl, F., and Heinig, K., "Active control of fan noise from high-bypass ratio aeroengines: a numerical study," *The Aeronautical Journal*, Vol. 105, No. 1053, 2001, pp. 627–631. https://doi.org/https://doi.org/10.1017/S0001924000012628.

[21] Enghardt, L., Tapken, U., Neise, W., Schimming, P., Maier, R., and Zillmann, J., "Active control of fan noise from high-bypass ratio aeroengines: experimental results," *The Aeronautical Journal*, Vol. 106, No. 1063, 2002, p. 501–506. https://doi.org/10.1017/S0001924000092356.

[22] Pagès, V., Duquesne, P., Aubert, S., Blanc, L., Ferrand, P., Ottavy, X., and Brandstetter, C., "UHBR Open-Test-Case Fan ECL5/CATANA," *International Journal of Turbomachinery, Propulsion and Power*, Vol. 7, No. 2, 2022. https://doi.org/10.3390/ijtpp7020017.

[23] Schonfeld, T., and Rudgyard, M., "Steady and unsteady flow simulations using the hybrid flow solver AVBP," *AIAA Journal*, Vol. 37, No. 11, 1999, pp. 1378–1385. https://doi.org/10.2514/2.636.

[24] Al-Am, J., Giauque, A., Clair, V., Boudet, J., and Gea-Aguilera, F., "Direct-Noise of an Ultrahigh-Bypass-Ratio Turbofan: Periodic-Sector vs Full-Annulus Large-Eddy Simulations," *AIAA Journal*, Vol. 62, No. 8, 2024, pp. 2831–2845. https://doi.org/https://doi.org/10.2514/1.J063596.

[25] Moreau, S., "Turbomachinery-related aeroacoustic modelling and simulation," *Proceedings of 17th International Conference on Fluid Flow Technologies*, 2018, pp. 1–15.

[26] Wang, G., Duchaine, F., Papadogiannis, D., Duran, I., Moreau, S., and Gicquel, L. Y., "An overset grid method for large eddy simulation of turbomachinery stages," *Journal of Computational Physics*, Vol. 274, 2014, pp. 333–355. https://doi.org/10.1016/j.jcp.2014.06.006.

[27] Colin, O., and Rudgyard, M., "Development of high-order Taylor-Galerkin schemes for LES," *Journal of Computational Physics*, Vol. 162, No. 2, 2000, pp. 338–371. https://doi.org/10.1006/jcph.2000.6538.

[28] Nicoud, F., Toda, H. B., Cabrit, O., Bose, S., and Lee, J., "Using singular values to build a subgrid-scale model for large eddy simulations," *Physics of fluids*, Vol. 23, No. 8, 2011. https://doi.org/10.1063/1.3623274.

[29] Poinsot, T., and Lele, S., "Boundary conditions for direct simulations of compressible viscous flows," *Journal of Computational Physics*, Vol. 101, No. 1, 1992, pp. 104–129. https://doi.org/10.1016/0021-9991(92)90046-2.

[30] Schmitt, P., Poinsot, T., Schuermans, B., and Geigle, K. P., "Large-eddy simulation and experimental study of heat transfer, nitric oxide emissions and combustion instability in a swirled turbulent high-pressure burner," *Journal of Fluid Mechanics*, Vol. 570, 2007, pp. 17–46. https://doi.org/10.1017/S0022112006003156.

[31] Al-Am, J., Clair, V., Giauque, A., Boudet, J., and Gea-Aguilera, F., "A Parametric Study on the LES Numerical Setup to Investigate Fan/OGV Broadband Noise," *International Journal of Turbomachinery, Propulsion and Power*, Vol. 6, No. 2, 2021. https://doi.org/10.3390/ijtpp6020012.

[32] Lewis, D., Moreau, S., Jacob, M. C., and Sanjosé, M., "ACAT1 fan stage broadband noise prediction using large-eddy simulation and analytical models," *AIAA Journal*, Vol. 60, No. 1, 2022, pp. 360–380. https://doi.org/10.2514/1.J060163.

[33] Munjal, M. L., *Acoustics of ducts and mufflers with application to exhaust and ventilation system design*, John Wiley & Sons, 1987.